Separation Science and Technology
Publication details, including instructions for authors and subscription information:
http://www.tandfonline.com/loi/lsst20

Numerical Analysis of Drops Coalescence and Breakage Effects on De-Oiling Hydrocyclone Performance

S. Noroozi [a] , S. H. Hashemabadi [a] & A. J. Chamkha [b]

[a] Computational Fluid Dynamics Research Laboratory, School of Chemical Engineering, Iran University of Science and Technology, Tehran, Iran

[b] Manufacturing Engineering Department, The Public Authority for Applied Education & Training, Shuweikh, Kuwait

Accepted author version posted online: 07 Jan 2013.Version of record first published: 27 Mar 2013.

To cite this article: S. Noroozi , S. H. Hashemabadi & A. J. Chamkha (2013): Numerical Analysis of Drops Coalescence and Breakage Effects on De-Oiling Hydrocyclone Performance, Separation Science and Technology, 48:7, 991-1002

To link to this article: http://dx.doi.org/10.1080/01496395.2012.752750

Separation Science and Technology, 48: 991–1002, 2013

ISSN: 0149-6395 print/1520-5754 online
DOI: 10.1080/01496395.2012.752750

Taylor & Francis
Taylor & Francis Group

Numerical Analysis of Drops Coalescence and Breakage Effects on De-Oiling Hydrocyclone Performance

S. Noroozi,[1] S. H. Hashemabadi,[1] and A. J. Chamkha[2]

[1]*Computational Fluid Dynamics Research Laboratory, School of Chemical Engineering, Iran University of Science and Technology, Tehran, Iran*

[2]*Manufacturing Engineering Department, The Public Authority for Applied Education & Training, Shuweikh, Kuwait*

This work investigated the effects of breakage and coalescence on de-oiling hydrocyclone performance utilizing Computational Fluid Dynamics (CFD). It was found that an increase in the entrance flow rate with low entrance oil concentration not only did not increase the separation performance of the hydrocyclone but it also decreased the separation efficiency. On the contrary, the hydrocyclone performance was enhanced with increasing the inlet velocity. Furthermore, a comparison between the standard design and the conical inlet chamber design was drawn in terms of separation efficiency for low entrance oil concentration; the results depicted that the conical design had higher separation efficiency.

Keywords coalescence; computational fluid dynamics (CFD); deoiling; droplets breakage; hydrocyclone

INTRODUCTION

Hydrocyclones are originally designed for solid-liquid separations, but at the present time they are also used for liquid-liquid and gas-liquid separations. Despite the common use of hydrocyclones, their exact design is often difficult because there exist many mathematical relationships to predict the separation efficiency and the pressure drop based on semi-empirical models. Moreover, these correlations are restricted to particular cyclone geometry and operating conditions. In recent years, applications of long liquid-liquid hydrocyclone have been extended in many ways. Some specific features of hydrocyclones such as low maintenance cost due to the lack of moving parts, simple operation, and installation make them proper and functional devices for separation processes.

Some CFD simulations of liquid-liquid flow through hydrocyclones have been published in which the droplet-droplet interactions have been ignored. Grady et al. (1) utilized the RSM turbulence and algebraic slip mixture model for the calculation of the velocity field and separation efficiency in 10 mm de-oiling hydrocyclone. Paladino et al. (2) applied similar methods for multiphase flow simulation in low oil concentration at the hydrocyclone feed. Huang (3) used the RSM (Reynolds Stress Model) model for modeling turbulent flow and Eulerian-Eulerian approach for the prediction of flow behavior in high concentration of oil in the entrance feed through the Colman-Thew hydrocyclone type. Noroozi and Hashemabadi (4) studied numerically the influence of different inlet designs on the de-oiling hydrocyclone efficiency. In another work, Noroozi and Hashemabadi (5) investigated the inlet chamber body profile effects on de-oiling hydrocyclone efficiency utilizing CFD simulation. Their results show that the separation efficiency can be improved with appropriate hydrocyclone body design.

Separation processes in liquid-liquid systems with turbulent flow are affected by shear forces that can cause the droplet to break and coalesce. This phenomenon can bring about the droplet size distribution change which has a great effect on separation efficiency. A transient droplet size distribution is modeled utilizing population balance equations coupled with momentum equations. CFD simulations of droplet coalescence and breakage in turbulent flows have been attempted for the prediction of separation efficiency in liquid-liquid industrial processes in the literature.

Alopaeus et al. (6) used population balance coupled with turbulent flow equations to develop a drop population model in a stirred tank. Lasheras et al. (7) considered the statistical description of the break-up of an immiscible fluid lump immersed into a fully developed turbulent flow. In their work, particle fragmentation was caused only by turbulent velocity fluctuations. Vikhansky et al. (8) proposed an extension of the Euler-Lagrangian approach for liquid–liquid two phase flows in a highly dispersed phase volume fraction. Attarakiha et al. (9) developed a numerical

Received 21 June 2012; accepted 21 November 2012.

Address correspondence to Seyed Hassan Hashemabadi, Computational Fluid Dynamics Research Laboratory, School of Chemical Engineering, Iran University of Science and Technology, 16846, Tehran, Iran. Fax: +(9821) 7724-0495. E-mail: hashemabadi@iust.ac.ir

algorithm to solve the PBE (Population Balance Equation) for considering the hydrodynamics of interacting liquid–liquid dispersions and droplet interactions (breakage and coalescence). Andersson et al. (10) studied the effect of turbulence on droplet size distributions in a novel multiphase reactor. In this work, they studied the wide range of turbulence intensities for different dispersed phase hold-ups. Schmidt et al. (11) studied the hydrodynamic and mass transfer behavior of a rotary disc column (RDC) based on a population balance model. Hu et al. (12) used the population balance equations to predict phase inversion in liquid–liquid dispersed pipeline flows. Kankaanpaa (13) considered the coalescence and breakage in a solvent extraction settler system with the aim of optimizing the design parameters. Patrunoa et al. (14) considered four different breakage kernels in order to predict a size distribution in a stirrer tank including a benzene–carbon tetrachloride mixture.

There exist a few experimental and numerical studies of droplet breakage and coalescence effect on the separation efficiency in liquid-liquid hydrocyclones. Meyer and Bohnet (15) investigated the effect of breakage and coalescence of oil droplets in different feed oil concentration and entrance mean droplet size on the separation efficiency for a de-oiling hydrocyclone. Schutz et al. (16) studied the coalescence and breakage effects in a de-watering hydrocyclone utilizing a CFD method. Furthermore, in this study they considered the effect of the structure and two inlet designs on droplet size distribution through the hydrocyclone.

In the present investigation, the effects of different feed mass flow rates, inlet droplet size distributions and entrance oil concentration on droplets breakage and coalescence were considered; the influence of these factors on the hydrocyclone separation efficiency was studied, as well. Furthermore, the effect of a conical entrance chamber compared to the standard design has been discussed in terms of separation efficiency, breakage and coalescence of droplets.

MATHEMATICAL FORMULATION

The continuity equations for both the water and oil phases are expressed respectively as follows:

$$\frac{\partial(\alpha_{Co}\rho_{Co})}{\partial t} + \nabla \cdot (\alpha_{Co}\rho_{Co}u_{Co}) = 0 \tag{1}$$

$$\frac{\partial(\alpha_{d}\rho_{d})}{\partial t} + \nabla \cdot (\alpha_{d}\rho_{d}u_{d}) = 0 \tag{2}$$

where the subscripts Co and d represent continuous and dispersed phases (here water and oil), respectively, and α is the volume fraction. The coalescence and breakage of oil droplets are computed as source terms in the oil phase continuity equation. In this study, the dispersed phase was assumed to be made of several numbers of particle classes (size groups). This was done in order to consider the oil droplets coalescence and breakage. The droplet breakage and coalescence are taken into account as mass transfer source terms in the continuity equations. Moreover, the breakage and coalescence of droplets is specified as mass transfer of each size group into the other ones. Moreover, similar properties have been assumed for all size groups (13). The continuity equation for each size group is represented as follows:

$$\frac{\partial(\alpha_{d,i}\rho_{d}f_{i})}{\partial t} + \nabla \cdot (\alpha_{d,i}\rho_{d}u_{d}f_{i}) = S_{i} \tag{3}$$

where f_i is the fraction of the dispersed phase volume fraction for each size group ($\alpha_{d,i}=f_i\ \alpha_d$). S_i is the source term of interphase mass transfer including birth and death rate of dispersed phase droplets due to breakage and coalescence which can be symbolized as below:

$$S_i = B_B - D_B + B_C - D_C \tag{4}$$

where B_B and B_C represent the birth rate and D_B and D_C imply the death rate of droplets due to breakage and coalescence, respectively (13). It is worth noting that although the volume of oil in each droplet range through breakage and coalescence is changing, the total volume of oil remains the same and therefore the sum of all droplet volume fractions equals to the volume fraction of dispersed phase which can be given by:

$$\sum_i \alpha_{d,i} = \alpha_d \tag{5}$$

Breakage Simulation

Since droplet breakup processes are complicated in turbulent flows, simplifications of the processes and flow conditions are crucial. The first assumption is the binary breakup of particles: a particle breaks into two daughter particles with equal or unequal sizes. The second one is that the particle size lies in the inertial sub-range: characteristics of particle and eddy motion in turbulent flows can be expressed as a function of the dissipation rate only (17).

The breakage is defined by the probability function, which is based on the energy level of the arriving eddies. The droplet breakage only occurs when the length scale of eddies is equal or smaller than the droplet diameter. The breakage rate of droplets with volume ν_j (size d_j) into droplets with volume ν_i (size d_i) can be expressed by (17,18, and 19):

$$\Omega_B(\nu_j : \nu_i) = \int_{\lambda_{\min}}^{d} P_B(\nu_j : \nu_i, \lambda)\, \omega_{B,\lambda}(\nu_j)\, d\lambda \tag{6}$$

where $\omega_{B,\lambda}$ is the collision density of eddies of size between λ and $\lambda + d\lambda$ on droplets of volume ν_j. The P_B (ν_j: ν_i, λ) is the probability for a droplet of volume ν_j to break into two droplets with volumes of ν_i ($\nu_i = \nu_j f_{BV}$) and ν_h. λ_{min} is the minimum eddy size which has the energy required for droplet breakage. The breakage volume fraction, f_{BV}, can be defined in binary break-up as follows:

$$f_{BV} = \frac{\nu_i}{\nu_j} = \frac{d_i^3}{d_j^3} = \frac{d_i^3}{d_i^3 + d_h^3} \tag{7}$$

where d_i and d_h are diameters of the daughter droplets of the parent droplet with diameter d_j. The specific droplet breakage rate is obtained when the break-up model is calibrated by the coefficient f_B and when Eq.6 is altered per the number of droplets yielding:

$$g(\nu_j : \nu_i) = f_B \Omega_B(\nu_j : \nu_i) \frac{1}{n} \tag{8}$$

In this work, the Luo and Svendsen approach (17,18) has been used for computing the eddy collision density. Luo and Svendsen (18) defined the collision frequency of eddies of a size between λ and $\lambda + d\lambda$ with droplets of size d in the inertial sub-range of isotropic turbulence. It can be written for a droplet d_j as follows:

$$\omega_{B,\lambda}(d_j) = 0.923\, n\, (1 - \alpha_d)(\varepsilon)^{1/3} \frac{(1+\xi)^2}{d_j^2 \xi^{11/3}} \tag{9}$$

where ξ is the dimensionless size ratio of an eddy and droplet ($\xi = \lambda / d_j$). The breakage probability of a droplet is equal to probability of the arriving eddy with size λ which has a kinetic energy level greater or equal than the minimum energy required for droplet breakage expressed as follows:

$$P_B(\nu_j : \nu_i, \lambda) = \exp(-\chi_c) = \exp\left(-\frac{12(f_{BV}^{2/3} + (1 - f_{BV})^{2/3} - 1)\sigma}{\beta \rho_c \varepsilon^{2/3} d_j^{5/3} \xi^{11/3}} \right) \tag{10}$$

where χ_c is the critical dimensionless energy for breakage and β is the empirical parameter from the turbulence theory which is equal to 2.0 in this model and σ demonstrates the surface tension between oil and water. As a result, the break-up frequency of a mother droplet with size d_j splitting in two droplets of sizes d_i and $d_h = (d_j^3 - d_i^3)^{1/3}$ is given by:

$$g(\nu_j : \nu_i) = 0.923 f_B (1 - \alpha_d)(\frac{\varepsilon}{d_j^2})^{1/3} \int_{\xi_{min}}^{1} \frac{(1+\xi)^2}{\xi^{11/3}}\, e^{-X_c}\, d\xi \tag{11}$$

where ξ_{min} is the dimensionless minimum size of eddies in the inertial sub-range of isotropic turbulence and is defined by $\xi_{min} = \lambda_{min}/d_j$. Thus, $\xi_{min} = 11.4\eta/d_j$, in which η is the Kolmogorov length-scale ($\eta = [(\mu_c/\rho_c)^3/\varepsilon]^{1/4}$). Accordingly, the birth and death rate due to the larger droplets can be obtained by the following equations:

$$B_B = \rho_d\, \alpha_d\, (\sum_{j>i} g(v_j; v_i) f_i) \tag{12}$$

$$D_B = \rho_d\, \alpha_d\, (f_i \sum_{j>i} g(v_j; v_i)) \tag{13}$$

Coalescence Simulation

In this study, droplet coalescence is computed using the Prince and Blanch approach (20). This model is based on the turbulence dissipation of the continuous phase. In this model, the coalescence process has been assumed to take place in three steps which have been shown schematically in Fig. 1. At the first step, a small amount of continuous phase is entrapped between the droplets. Second, this liquid film is drained until it reaches the critical thickness and finally, the critical film thickness between two droplets ruptures and coalescence takes place.

In the Prince and Blanch approach (20), the coalescence frequency of particles with volume v_i to particles with volume v_j for the formation of particles with volume of $(v_i + v_j)$ can be calculated by the following expression:

$$C(v_i; v_j) = Z\, A_{ij} \left[(u_i^t)^2 + (u_j^t)^2 \right]^{\frac{1}{2}} \exp(-t_{ij}/T_{ij}) \tag{14}$$

where Z is the calibration factor and A_{ij} represents the cross-sectional area of the colliding droplets expressed as follows:

$$A_{ij} = \frac{\pi}{4}(d_i + d_j)^2 \tag{15}$$

It should be noted that u_i^t and u_j^t appearing in Eq. (14) represent the turbulence velocities that can be assessed by:

$$u_i^t = \sqrt{2}\varepsilon^{1/3} d_i^{1/3}, \quad u_j^t = \sqrt{2}\varepsilon^{1/3} d_j^{1/3} \tag{16}$$

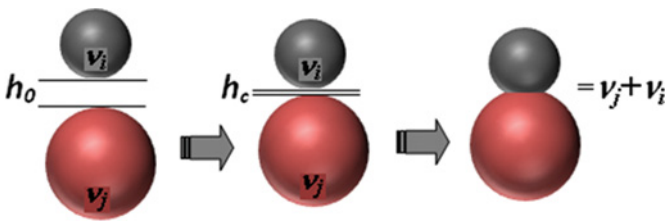

FIG. 1. Schematic diagram of coalescence stages. (Color figure available online)

Moreover, t_{ij} in Eq. (14) is the time required for the coalescence of droplets of radius r_i and r_j and T_{ij} is the contact time for the two particles which can be evaluated, respectively by the following terms:

$$t_{ij} = \left(\frac{\rho_c r_{ij}^3}{16\sigma}\right)^{1/2} \ln\left(\frac{h_0}{h_{cr}}\right) \tag{17}$$

$$T_{ij} = \frac{r_{ij}^{2/3}}{\varepsilon^{1/3}} \tag{18}$$

where h_0 and h_{cr} are the initial and critical film thicknesses when rupture takes place, respectively. Initial film thickness and critical film thickness at which rupture occurs were set to 1×10^{-4} m and 1×10^{-8} m in this study. Furthermore, the equivalent radius r_{ij} can be obtained as follows:

$$r_{ij} = \frac{d_i d_j}{d_i + d_j} \tag{19}$$

As a final point, the birth and death rate of coalescence are defined as follows:

$$B_C = (\rho_d \alpha_d)^2 \left(\frac{1}{2}\sum\sum Q(v_j; v_k) X_{jki} f_j f_k \frac{m_j + m_k}{m_j m_k}\right) \tag{20}$$

$$D_C = (\rho_d \alpha_d)^2 \left(\sum Q(v_j; v_k) f_i f_j \frac{1}{m_j}\right) \tag{21}$$

where X_{jki} is the coalescence mass matrix that is defined as the fraction of mass due to coalescence between groups j which goes into group i(13):

$$X_{jki} = \begin{cases} \frac{(m_j+m_k)-m_{i-1}}{m_i-m_{i-1}} & if \quad m_{i-1} < m_j + m_k < m_i \\ \frac{m_{i+1}-(m_j+m_k)}{m_{i+1}-m_i} & if \quad m_i < m_j + m_k < m_{i+1} \\ 0 & otherwise \end{cases} \tag{22}$$

The Simulation Method for Liquid-Liquid Flow

In the current study, the liquid-liquid two-phase flow is simulated utilizing an Eulerian-Eulerian approach. In this approach, each phase is considered as a continuum and described by averaged conservation equations. For incompressible fluids, the averaged momentum equations for each phase (oil or water) may be obtained from the following equation (21):

$$\frac{\partial(\alpha_p \rho_p u_p)}{\partial t} + u_p \nabla.(\alpha_p \rho_p u_p) = \alpha_p \nabla p - \nabla.[\alpha_p(\tau_p^l + \tau_p^t)] + \alpha_p \rho_p g + F_M \tag{23}$$

where g is the gravitational body force and p is the static pressure. Moreover, the subscript 'p' is substituted by 'c' for the water phase (as continuous phase) and 'd' for oil phase (as dispersed phases). F_M is the interphase momentum exchange or transfer term between the two phases which is composed of all the correlated interphase forces such as drag, lift, virtual mass, and turbulent dispersion forces.

In this work due to the small diameter of droplets and the assumptions of spherical shape, the shear-lift force and the lift force caused by slanted wakes can be discounted (22). Also, because of very low concentration of oil in the feed and therefore a very low concentration of oil in the vicinity of the walls, the wall-lift (wall-lubrication) force was eliminated (22 and 23). Further, due to low density differences between two liquids, virtual mass force is also negligible. In view of these assumptions, only drag and turbulent dispersion forces were considered. Drag force can be calculated as follows (21):

$$F_{Drag} = \frac{3\alpha_d \alpha_c \rho_c C_D |u_d - u_c|(u_d - u_c)}{4 d_d} \tag{24}$$

On the grounds of the fact that the viscosity ratio of the two phases is very large ($\mu_{oil}/\mu_{water} = 28$), the drag coefficient can be obtained from the correlations based on a solid particle (4). In this work the following empirical Schiller-Naumann correlation (24) is used for evaluation of the drag coefficient:

$$C_D = \begin{cases} \frac{24}{Re_d}\left(1 + 0.15\, Re_d^{0.687}\right) & Re_d \le 1000 \\ 0.44 & Re_d > 1000 \end{cases} \tag{25}$$

where $\mathrm{Re_d}$ is the droplet Reynolds number defined as

$$Re_d = \frac{\rho_c |u_c - u_d| d_d}{\mu_c} \tag{26}$$

The interaction of drops dispersion due to turbulent flow is taken into account by the turbulent dispersion force given as follows (25).

$$\boldsymbol{F}_{td} = \boldsymbol{C}_{TD}\, \boldsymbol{C}_D \frac{\nu_{t,c}}{\sigma_{t,d}}\left(\frac{\nabla \alpha_d}{\alpha_d} - \frac{\nabla \alpha_c}{\alpha_c}\right) \tag{27}$$

where C_{TD} is the turbulent dispersion coefficient and $\nu_{t,c}$ is the turbulent kinematic viscosity for the continuous phase and $\sigma_{t,d}$ is the turbulent Schmidt number of dispersed phase. For the continuous phase, this force is equal but opposite in sign.

Turbulence Model

In this study, the Reynolds Stress Model (RSM) was chosen as the turbulence model. The RSM turbulence model is reported an effective and accurate model for

simulation of the velocity field through a hydrocyclone (26). The Reynolds stress model involves calculation of the individual turbulence stresses (R_{ij}) using partial differential transport equations:

$$\frac{\partial}{\partial t}(\rho R_{ij}) = \underbrace{-\rho\left(R_{ik}\frac{\partial u_j}{\partial x_k} + R_{jk}\frac{\partial u_i}{\partial x_k}\right)}_{P_{ij}} + \underbrace{\frac{\partial}{\partial x_i}\left(\mu\frac{\partial R_{ij}}{\partial x_i}\right) + C_\mu\frac{\partial}{\partial x_i}\left(\frac{\mu_t}{\sigma_k}\frac{\partial R_{ij}}{\partial x_i}\right) - \frac{\partial}{\partial x_i}(\rho u_i R_{ij})}_{D_{ij}} - \varepsilon_{ij} + \Phi_{ij} \quad (28)$$

where P_{ij} is the production of turbulence stresses and D_{ij} includes the molecular diffusion, turbulent diffusion and convection of turbulence stresses (R_{ij}). The kinetic energy dissipation rate tensor (ε_{ij}) which makes use of Kolmogrov assumption of local isotropy can be expressed as a function of scalar kinetic energy dissipation rate (ε), given by the following partial differential equation:

$$\varepsilon_{ij} = \frac{2}{3}\varepsilon\delta_{ij} \quad (29)$$

$$\frac{\partial \varepsilon}{\partial t} + \frac{\partial}{\partial x_i}(u_i\varepsilon) = \frac{\partial}{\partial x_i}\left(C_\varepsilon\frac{\varepsilon}{k}R_{ij}\frac{\partial u_i}{\partial x_j}\right) - \frac{\varepsilon}{k}\left(2C_{\varepsilon 1}R_{ij}\frac{\partial u_i}{\partial x_i} + C_{\varepsilon 2}\varepsilon\right) \quad (30)$$

The final term in Eq. (29), Φ_{ij} simulates the re-distribution of turbulence by the pressure-strain gradient. Different alternatives are presented in the literature for calculation of this term, Φ_{ij}. In this work, the linear pressure strain gradient was used which can be given by the following expression:

$$\Phi_{ij} = -C_1\rho\frac{\varepsilon}{\kappa}\left(R_{ij} - \frac{2}{3}\delta_{ij}\kappa\right) - C_2\left(P_{ij} - \frac{2}{3}\delta_{ij}G_k\right) \quad (31)$$

where all of the constants that were used in this work for the RSM model equations are presented in Table 1.

TABLE 1
Constants for the RSM turbulence model equations

RSM model constants	C_μ	C_1	C_2	$C_{\varepsilon 1}$	$C_{\varepsilon 2}$	C_ε	σ_k	C_s
Value	0.24	−1.8	−0.6	1.4	1.92	0.13	0.82	0.09

HYDROCYCLONE GEOMETRIES, OPERATING, AND BOUNDARY CONDITIONS

Geometries

In this work, two different geometries were used for analysis of design effect on breakage and coalescence of oil droplets; Fig. 2 shows the geometry parameters for both designs in detail. The first design is according to the work of Meyer and Bohnet (15), and the second one is based on the first one in which the cylindrical inlet chamber has been substituted for the conical chamber (angle of 15°).

Inlet Droplet Size Distribution

The properties for water and oil (along with surface tension between oil and water) used in this study have been presented in Table 2. The inlet droplet size distributions were subdivided into 12 size groups with two volume mean diameters according to Meyer and Bohnet (15). Each discrete size fraction has been defined in Table 3. The mean droplet diameter in two different droplet size distributions ($d_{dsd,50}$), considered in this study, are 150 and 200 μm. Moreover, the droplet size distribution changes, due to the breakage and coalescence, were considered by making a comparison between entrance droplet size distribution and the so-called real droplet size distribution. The real droplet size distribution can be obtained from the drop size distribution at the underflow and overflow conditions represented as follows (15 and 16):

$$Q_{real}(d) = gQ_{overflow}(d) + fQ_{underflow}(d) \quad (32)$$

The f and g are the integral droplet volume fraction at the underflow and at the overflow, respectively.

In this simulation, the prescribed inlet velocity (3.2 m/s) at the inlet boundary condition was used as a plug flow. The imposed mass flow rate boundary condition regarding overflow split ratio R_f for outlets was set as a percentage of inlet mass flow rate (40 percent in this work). The wall boundaries were subjected to no slip conditions and the standard wall function was applied near the wall.

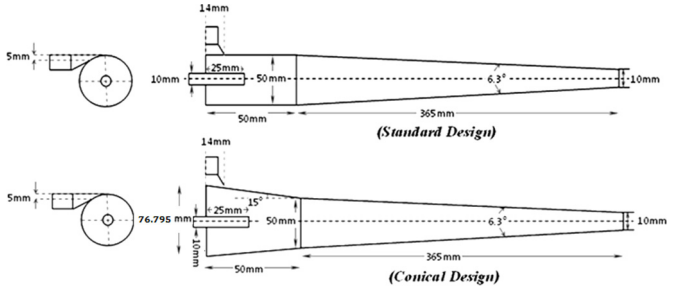

FIG. 2. Geometry details of two de-oiling hydrocyclones with different feed chamber.

TABLE 2
Physical properties of water and oil at 20°C

	Density (kg/m^3)	Viscosity (Pa.s)	Surface tension (N/m)
oil	845	28	45.9×10^{-3}
water	998	1	

For the sake of computational time reduction the structured hexahedral meshes were used. Moreover, by reason of flow and hydrocyclone geometry complexity, 200,000, 300,000, and 500,000 mesh densities for standard de-oiling hydrocyclones were examined and 300,000 mesh density was found as optimized mesh density in terms of accuracy and computational cost (the relative error of almost 3.75% compares to experimental error in terms of separation efficiency). Due to the high velocity gradient near the wall and central regions through the hydrocyclone, the grid was refined at these regions as shown in Fig. 3. It is worth noting that the selected mesh as optimum mesh density has been applied for all simulations. Furthermore, the coalescence and breakage phenomena are applied in this study as source terms in continuity equation and are not a criterion for mesh density.

The Semi-Implicit Pressure Linked Equations (SIMPLE) algorithm is applied for coupling the continuity and momentum equations for two-phase flows to gain the pressure field inside the hydrocyclone (24). The Quadratic Upstream Interpolation for Convective Kinetics (QUICK) scheme (26) is used for interpolation of variables from cell centers to faces of control volumes that are recommended for higher accuracy in complex flow like in hydrocyclone

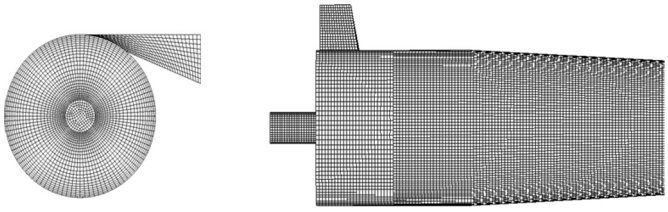

FIG. 3. Cross section of structured grid for hydrocyclone CFD simulation.

(27,28,29). Simulations are carried out for about 10,000 incremental steps and the time step is 0.001 s. The convergence criteria have been assigned 10^{-3} for all equations except the continuity equation and oil phase volumetric ratio at which the criteria are 10^{-5}.

RESULTS AND DISCUSSION

Model Verification

Prior to the application the numerical study of breakage and coalescence effect on oil-water separation efficiency through the hydrocyclone, it is compulsory to verify the models which are used in the simulation. To this aim, the breakage and coalescence effects on drop size distribution and separation efficiency in three different entrance oil drop size distributions was considered and the results were compared with the reported experimental data (15). The inlet velocity was constant (3.2 m/s) for the aforementioned conditions and the separation efficiency was defined as the ratio of oil flow rate at the overflow to feed flow rate (30), represented as follows:

$$E = \frac{\alpha_o q_o}{\alpha_{in} q_{in}} = 1 - \frac{\alpha_u q_u}{\alpha_{in} q_{in}} \tag{33}$$

TABLE 3
Discrete droplet size fraction (15)

Size group number i	$d_{dsd,50} = 150\,\mu m$	Particle number $d_{dsd,50} = 150\,\mu m$ (number/s)	$d_{dsd,50} = 200\,\mu m$	Particle number $d_{dsd,50} = 200\,\mu m$ (number/s)
1	15	1112866	36.5	2109058
2	40.1	4811489	73.8	113809
3	66.7	241781	92.7	122004
4	89	21978	127.3	36590
5	111.1	11338	157.9	21812
6	130.2	4968	195.8	10415
7	145.8	8534	234.6	4641
8	195.8	1892	268.8	2564
9	229.4	764	301	2381
10	256.9	752	352.8	1663
11	307.9	1556	432.5	634
12	431.5	3298	557.3	104

*droplet size distribution (dsd).

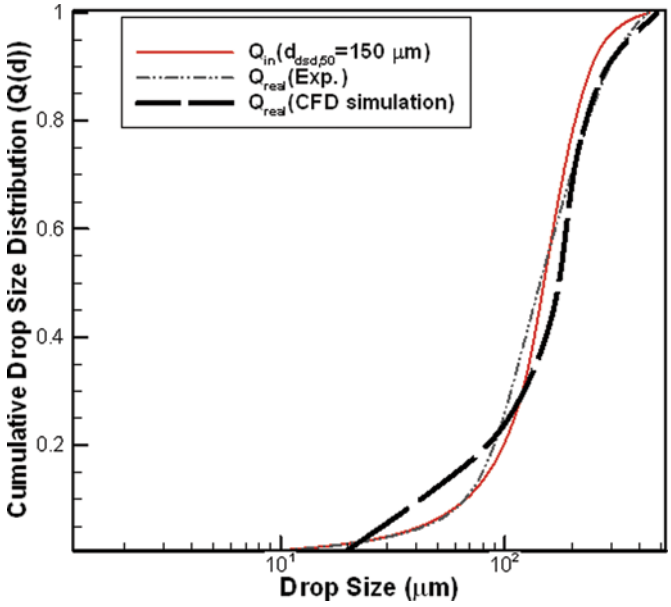

FIG. 4. Comparison the real droplet size distribution obtaining with CFD and experimental work [15], $d_{dsd,50,in} = 150\,\mu m$, $\alpha_{in} = 0.5\%$, $V_{in} = 3.2\,m/s$. (Color figure available online)

Figures 4 and 5 show the real cumulative droplet size distribution, Eq. (32), for two different entrance size distributions (150 and 200 micron) produced by CFD simulation in comparison with the experimental data (Meyer and Bohnet, 2003). According to these results the real size distributions in the two cases (Figs. 4 and 5) have appropriate agreement with the experimental results (the mean deviation of almost 17% compares to experimental records). Moreover, the results revealed that the breakage in the 200 micron mean entrance droplet size is more. The results also illustrate that the breakage of the small entrance diameter due to the small size of the droplets compared to the eddy size almost does not happen.

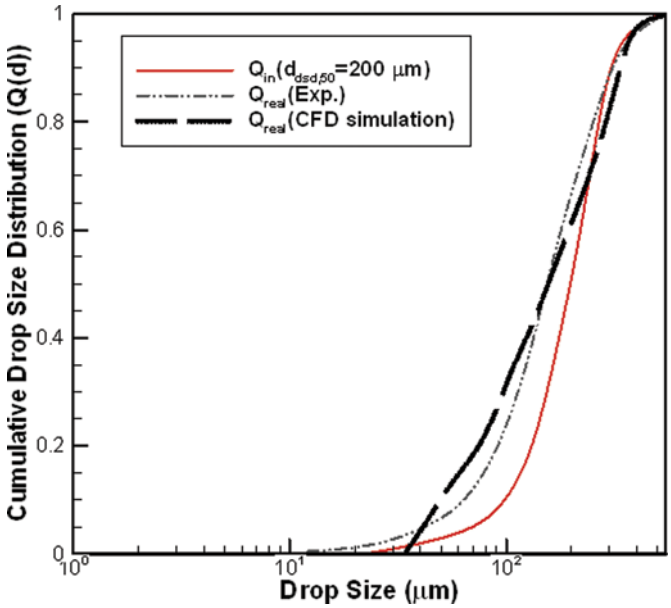

FIG. 5. Comparison the real droplet size distribution obtaining with CFD and experimental work [15], $d_{dsd,50,in} = 200\,\mu m$, $\alpha_{in} = 0.5\%$, $V_{in} = 3.2\,m/s$. (Color figure available online)

TABLE 4
Comparison of separation efficiency for two inlets mean droplet diameter ($\alpha_{in} = 0.5\%$, $V_{in} = 3.2\,m/s$

Entrance mean drop size distribution (μm)	Efficiency (CFD) (this work)	Efficiency (experimental) (Meyer and Bohnet, 2003)
150	0.95	0.93
200	0.87	0.92

Table 4 shows the separation efficiency obtained from the CFD simulation and the experimental work (Meyer and Bohnet, 2003) for two different entrance mean droplet diameters. The results depicted the appropriate agreement with experimental data (mean error of 3.75%). As shown in this table, the separation efficiency decreases with increasing values of the inlet mean droplet diameter because of more droplet breakage as mentioned by Meyer and Bohnet (2003). Overprediction for droplet breakage (Fig. 5) causes more reduction of efficiency compared to the experimental work.

Distribution of Size Groups in Hydrocyclone

Figure 6 (a, b) shows the contours of class distribution in a longitudinal cross section of the hydrocyclone for the

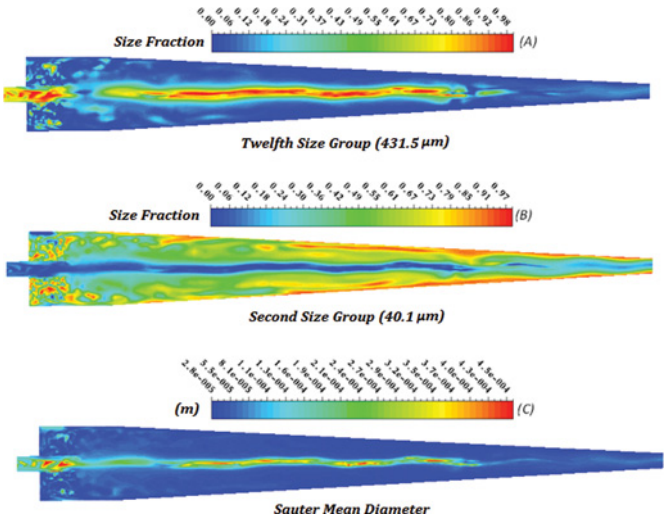

FIG. 6. Distribution of dispersed phase A) Twelfth size group, B) Second size group, and C) Droplets Sauter mean diameter ($d_{dsd,50,in} = 150\,\mu m$, $\alpha_{in} = 0.5\%$, $V_{in} = 3.2\,m/s$). (Color figure available online)

twelfth (Fig. 6a) and the second (Fig. 6b) size groups, respectively. As shown in Fig. 6a, the fraction of the twelfth size group is higher in the central regions concerning the other zones. It might be attributed to the migration of droplets from the wall to the central zone due to high centrifugal force which promotes droplet collision probability; this fact makes droplets coalescence higher in these zones. In contrast, it is visualized well (Fig. 6b) that the accumulation of droplets with 40 μm diameter (second size group) in the near wall region is higher than in other regions. This is related to droplet breakage rate in these regions because the high dissipation rates of fluid kinetic energy near the wall. Moreover, Fig. 6c shows the Sauter Mean Diameter (SMD) of droplets which illustrates the aggregation of coarse droplets in the central zone and fine ones near the wall.

Effect of High Entrance Oil Volume Fraction

Figure 7 shows the real cumulative size distribution for three different entrance size distributions for high oil volume fraction (15%) in the standard hydrocyclone design (Fig. 2). According to these results, it is seen that for high entrance oil volume fraction the coalescence effect is a dominant factor in two different entrance size distributions (150 and 200 μm). It might be related to the higher collision probability of droplets that leads to droplet coalescence in high oil volume fraction flows compared to the low oil volume fraction.

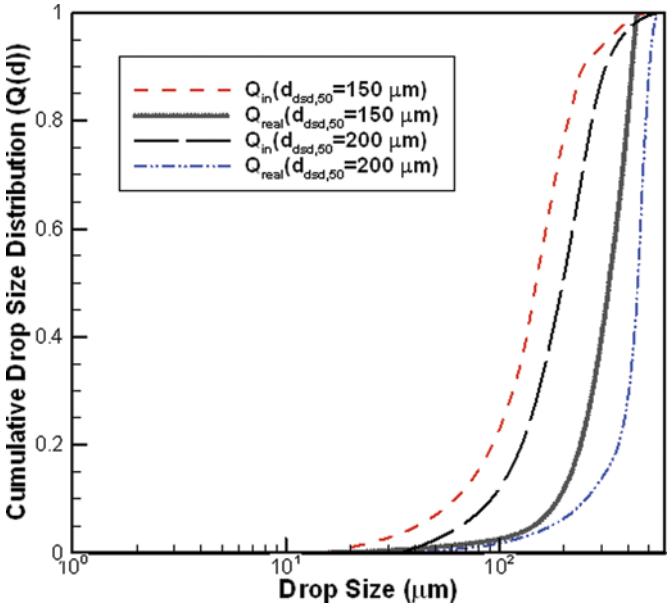

FIG. 7. Real cumulative size distribution for two different entrance size distributions in high volume fraction ($\alpha_{in} = 15\%$ oil) versus the inlet droplet size distribution ($V_{in} = 3.2$ m/s). (Color figure available online)

Effect of Inlet Velocity

Figures 8 and 9 show the radial distribution of the tangential velocity and turbulent eddy dissipation rate at 150 mm from the top wall of the standard hydrocyclone (Fig. 2) for different inlet velocities, respectively. The mean diameter of entrance droplet size distribution for all inlet velocities and entrance oil concentration are 150 μm and

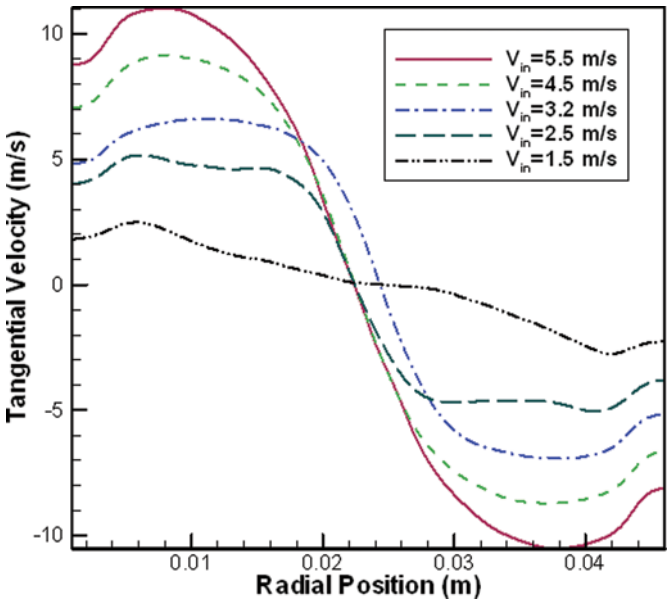

FIG. 8. Radial tangential velocity distribution in different inlet velocities at 150 mm from the top wall of standard hydrocyclone ($\alpha_{in} = 0.5\%$, $d_{dsd,50,in} = 150$ μm). (Color figure available online)

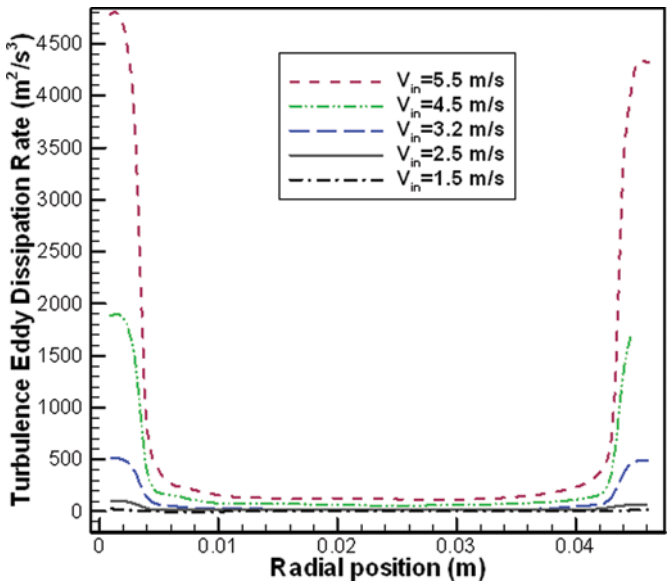

FIG. 9. Radial distribution of turbulence eddy dissipation rate in different inlet velocities at 150 mm from the top wall of standard hydrocyclone ($\alpha_{in} = 0.5\%$, $d_{dsd,50,in} = 150$ μm). (Color figure available online)

0.5%. As shown in these figures, increasing the inlet velocity enhances the tangential velocity which causes the separation efficiency to be promoted. In addition, increasing the inlet velocity causes the eddy dissipation rate to increase, which leads to higher droplet breakage especially in the regions near the wall due to the higher eddy dissipation rate. With respect to obtaining results, increasing the entrance velocity not only cannot lead to the enhancement of separation efficiency in each operational condition but it may result in reducing the separation efficiency due to the predominant effect of droplet breakage in high velocity zones through the hydrocyclone.

Figure 10 shows the real cumulative droplet size distribution for six entrance velocities utilizing CFD simulation for oil-water flow through the standard hydrocyclone (Fig. 2).The results depict that, although droplet breakage is more likely with high entrance velocities due to the high eddy dissipation rate in the vicinity of the wall; this phenomenon brings about the reduction of separation efficiency. Moreover, the tangential velocity is high in these ranges of inlet velocity which can result in enhanced of separation efficiency.

In contrast, in low velocity range, droplets breakage is minimal because of the lower effect of turbulence. But the lower tangential velocity can cause weaker back flow which leads to a reduction in the separation efficiency.

Figure 11 shows the separation efficiency at six different inlet velocities. As shown in this figure, the separation efficiency increases up to a point and then gradually starts to decrease with increasing the inlet velocity. It seems that the optimum operational conditions can be gained with an inlet flow rate which leads to the minimum breakage. At this operational condition the proper tangential velocity can be specified in which minimum drop breakage and high velocity to create strong back flow for separation of oil from water are met.

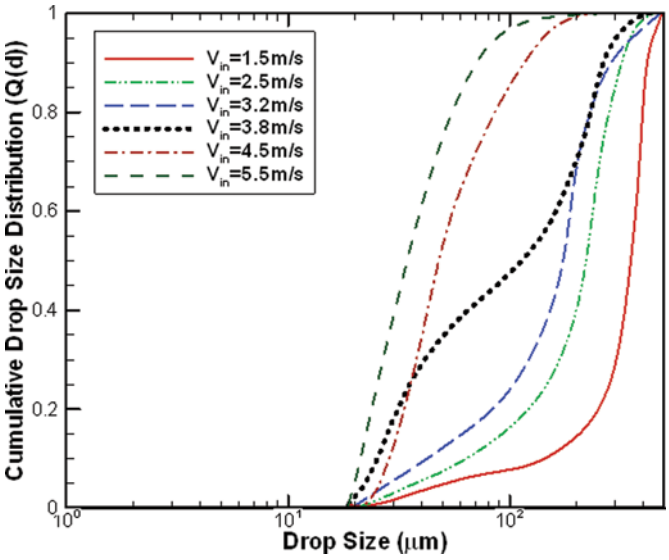

FIG. 10. Real cumulative size distribution for six different entrance velocities ($\alpha_{in} = 0.5\%$, $d_{dsd,50,in} = 150\,\mu m$). (Color figure available online)

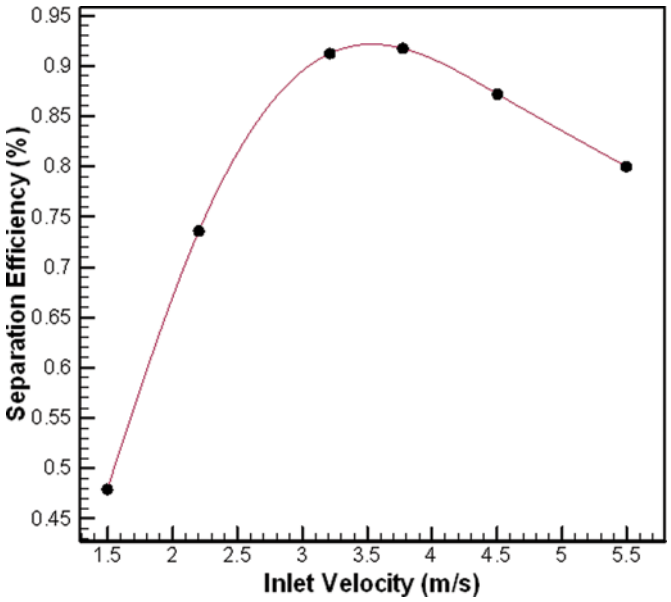

FIG. 11. Separation efficiency versus entrance velocity for standard design ($\alpha_{in} = 0.5\%$, $d_{dsd,50,in} = 150\,\mu m$). (Color figure available online)

Effect of Inlet Chamber Design

Owing to the fact that the separation efficiency decreases for large mean entrance droplet diameter in low

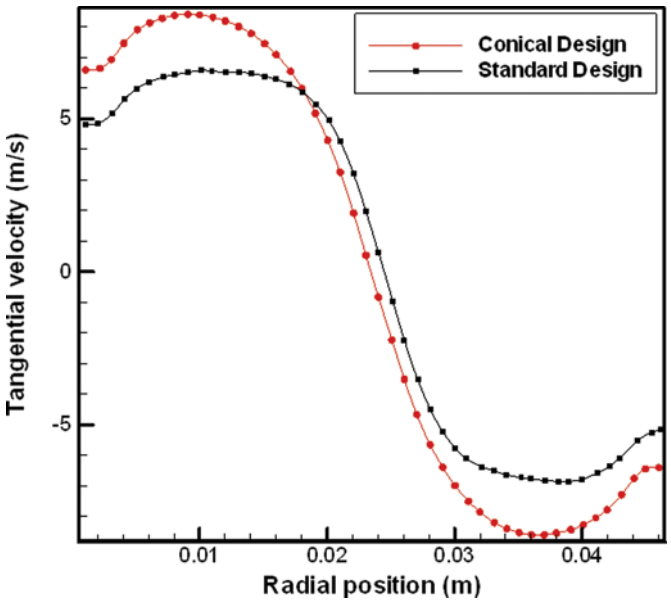

FIG. 12. Radial tangential velocity profile for two entrance chamber design at 150 mm from the top wall of standard and conical hydrocyclone ($\alpha_{in} = 0.5\%$, $d_{dsd,50,in} = 200\,\mu m$, $V_{in} = 3.2\,m/s$). (Color figure available online)

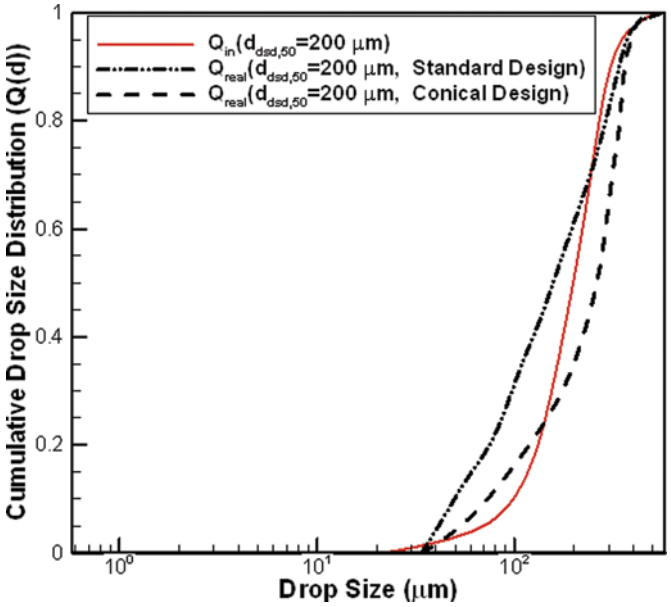

FIG. 13. Real cumulative size distribution for two different designs ($\alpha_{in} = 0.5\%$, $d_{dsd,50,in} = 200\,\mu m$, $V_{in} = 3.2\,m/s$). (Color figure available online)

oil concentration at high inlet velocities, the effect of conical inlet chamber design (Fig. 2) compared to the standard one was investigated with these conditions in this study. Figure 12 shows the tangential velocity profile in radial direction at 150 mm from the top wall of the hydrocyclone for the two different designs. The results show that the conical design creates higher tangential velocity through the hydrocyclone with the same inlet velocity. This might be attributed to the stronger eddy recirculation effect in the entrance chamber of the standard design (Noroozi and Hashemabadi, 2011) which causes more breakage through more dissipation of energy in this region. Increasing of tangential velocity in conical design compared to standard one causes the droplets to shift more to the central region due to the higher acceleration forces, which result in more accumulation of droplets in these regions. Figure 13 illustrates the real cumulative drop size distribution for two different hydrocyclone designs (Fig. 2). The results reveal that the droplet breakage effect decreases considerably in the case of the conical design. In addition, contrary to the standard design, the coalescence is the dominant phenomenon in the conical design. Therefore, it can be concluded that the conical inlet chamber design produces higher efficiency compared to the standard one for low oil concentration in the inlet water.

CONCLUSION

In this investigation, the effects of droplets breakage and coalescence on the separation efficiency of a de-oiling hydrocyclone were considered utilizing a CFD method. The Eulerian-Eulerian multiphase approach and the RSM turbulence model were applied for the prediction of phase distribution and understanding the hydrodynamics of flow through the hydrocyclone. In order to take account of the droplet-droplet interactions, the population balance equation was solved along with the momentum equation simultaneously. Furthermore, the Luo-Svendsen and Prince and Blanch approaches were used for the prediction of breakage and coalescence of droplets in each domain, respectively. With the aim of verification of the employed methods, the results were compared with reported experimental data (Meyer and Bohnet, 2003). The mean deviation of CFD results from the experimental data was approximately 17%. In addition, the effect of oil concentration in coalescence and breakage of the droplets was studied. The results illustrated that increased feed oil concentration enhanced breakage reduction due to increasing the droplet collision. Therefore, this effect can augment separation efficiency. Additionally, the effect of the inlet velocity was also studied on the breakage and coalescence for achieving the optimized velocity. The results showed that an increase in the entrance flow rate for low entrance oil concentration can decrease the separation efficiency because of the dominant droplet breakage effect. In addition, the effect of the conical chamber design on droplet breakage was also considered. According to the results, using the conical entrance chamber leads to increasing tangential velocity compared to standard one; this can increase the separation efficiency due to more drops migrating to the central regions.

ACKNOWLEDGEMENTS

We would like to express our gratitude to National Iranian Oil Products Distribution Company for financial supports.

NOMENCLATURE

A	[m^2] Cross-sectional area of the colliding droplets
B	[$kg.m^{-3}.s^{-1}$] Droplet birth term
C	[$m^3.\ s^{-1}$] Specific droplet coalescence rate
d	[m] Droplet diameter
D	[$kg.m^{-3}.s^{-1}$] Droplet death term
E	[%] De-oiling efficiency
F	[$N.\ m^{-3}$] Interphase momentum transfer term
g	[s^{-1}] Specific Droplet Break-up Rate
f_{BV}	[-] Breakage volume fraction
f_B	[-] Calibration coefficient of the breakage
f_i	[-] Fraction of dispersed phase volume fraction for each Size group
G_k	[$J.\ s^{-1}$] Generation of turbulent kinetic energy
h	[m] Film thickness

k	[-] Viscosity ratio of dispersed phase to continuous phase
L	[mm] Length
m	[Kg] Mass
n	[-] Number of droplets
P_B	[-] Breakage probability of a droplet
p	[N.m^{-2}] Static pressure
Q	[m^3.s^{-1}] Specific Droplet Coalescence Rate
$Q(d)$	[-] Cumulative drop size distribution
q	[m^3. s^{-1}] Flow rate
Re	[-] Reynolds number
R_{ij}	[N] Reynolds stresses
r_{ij}	[m] Equivalent radius
S_i	[kg. m^{-3}.s^{-1}] Mass transfer rate source term due to breakage and coalescence
T	[s] Contact time
t	[s] Time
u	[m.s^{-1}] Velocity
x	[-] Coordinates
Z	[-] Calibration coefficient of the coalescence

Greek Symbols

α	[%] Volume fraction
β	[-] Constant parameter in Eq. (10)
χ_c	[-] Critical dimensionless energy for droplet breakage
δ_{ij}	[-] Kronecker delta
ε	[J.s^{-1}] Turbulent kinetic energy dissipation rate
Γ_{ij}	[m^{-3}.s^{-1}] Coalescence rate
η	[m] Kolmogrov length scale
κ	[J] Tturbulent kinetic energy
λ	[m] Eddy size
μ	[kg. m^{-1}.s^{-1}] Dynamics viscosity
θ_{ij}^t	[m^{-3}.s^{-1}] Collision rate due to turbulence
ρ	[Kg. m^{-3}] Density
σ	[N.m^{-1}] Interfacial tension
τ	[pa] Stress tensor
Ω_B	[m^{-3}.s^{-1}] Breakage rate
$\omega_{B,\lambda}$	[m^{-4}.s^{-1}] Collision density
ξ	[-] Eddy/droplet size ratio

Subscripts

0	Initial
B	Breakage
C	Coalescence
c	Continuous phase
cr	Critical
d	Dispersed phase
i, j, k	Coordinate directions
in	Inlet
h	Daughter droplet diameter
M	Momentum
m	Mean
max	Maximum value
min	Minimum value
O	Overflow orifice
real	Real droplet size distribution
td	Turbulence Dispersion
U	Underflow orifice

Superscript

L	Laminar
t	Turbulent

REFERENCES

1. Grady, S.A.; Wesson, G.D.; Abdullah, M.; Kalu, E.E. (2003) Prediction of 10-mm hydrocyclone separation efficiency using computational fluid dynamics. *Filtr. Sep.*, 40 (9): 40.
2. Paladino, E.E.; Nunes, G.C.; Schwenk, L. (2005) CFD analysis of the transient flow in a low-oil concentration hydrocyclone. *Proc. of the Ann. Meeting AIChE*, Cincinnati, OH, USA.
3. Huang, S. (2005) Numerical simulation of oil-water hydrocyclone using Reynolds-Stress Model for Eulerian multiphase flows. *Can. J. Chem. Eng.*, 83: 829.
4. Noroozi, S.; Hashemabadi, S.H. (2009) CFD Simulation of inlet design effect on de-oiling hydrocyclone separation efficiency. *Chem. Eng. Technol*, 32 (12): 1885.
5. Noroozi, S.; Hashemabadi, S.H. (2011) CFD analysis of inlet chamber body profile effects on de-oiling hydrocyclone efficiency. *Chem. Eng. Res. Des.*, 89: 968.
6. Alopaeus, V.; Koskinen, J.; Keskinen, K.I. (1999) Simulation of the population balances for liquid-liquid systems in a non-ideal stirred tank. Part 1 Description and qualitative validation of the model. *Chem. Eng. Sci.*, 54: 5887.
7. Lasheras, J.C.; Eastwood, C.; Bazan, C.M.; Montanes, J.L. (2002) A review of statistical models for the break-up of an immiscible fluid immersed into a fully developed turbulent flow. *Int. J. Multiphase Flow*, 28: 247.
8. Vikhansky, A.; Kraft.M. (2004) Modelling of a RDC using a combined CFD-population balance approach. *Chem. Eng. Sci.*, 59: 2597.
9. Attarakiha, M.M.; Bart, H.J.O.; Faqir, N.M. (2004) Numerical solution of the spatially distributed population balance equation describing the hydrodynamics of interacting liquid–liquid dispersions. *Chem. Eng. Sci.*, 59: 2567.
10. Andersson, R.; Andersson, B.; Chopard, F.; Norén, T. (2004) Development of a multi-scale simulation method for design of novel multiphase reactors. *Chem. Eng. Sci.*, 59: 4911.
11. Schmidt, S.A.; Simon, M.; Attarakih, M.M.; Lagar L.; Bart H.J. (2006) Droplet population balances modeling: hydrodynamics and mass transfer. *Chem. Eng. Sci.*, 61: 246.
12. Hu, B.; Matar, O.K.; Hewitt, G.F.; Angeli, P. (2006) Population balance modeling of phase inversion in liquid–liquid pipeline flows. *Chem. Eng. Sci.*, 61: 4994.
13. Kankaanpaa, T. (2007) CFD procedure for studying dispersion flows and design optimization of the solvent extraction settler. Doctoral Thesis, *Helsinki University of technology*.
14. Patrunoa, L.E.; Doraob, C.A.; Svendsena, H.F.; Jakobsena, H.A. (2009) Analysis of breakage kernels for population balance modeling. *Chem. Eng. Sci.*, 64: 501.
15. Meyer, M.; Bohnet, M. (2003) Influence of entrance droplet size distribution and feed concentration on separation of immiscible liquids using hydrocyclones. *Chem. Eng. Technol.*, 26 (6): 660.

16. Schutz, S.; Gorbach, G.; Piesche, M. (2009) Modeling fluid behavior and droplet interactions during liquid–liquid separation in hydrocyclones. *Chem. Eng. Sci.*, 64: 3935.
17. Daeseong, J.; Shripad, T.R. (2011) Investigation of bubble breakup and coalescence in a packed-bed reactor – Part 1: A comparative study of bubble breakup and coalescence models. *Int. J. Multiphase Flow*, 37: 995.
18. Luo, H.; Svendsen, H.F. (1996) Theoretical model for drop and bubble break up in turbulent dispersions. *AIChE J.*, 42 (5): 1225.
19. Valdepenas, J.M.M.; Jimenez, M.A.; Barbero, R.; Martin Fuertes, F. (2007) A CFD comparative study of bubble break-up models in a turbulent multiphase jet. *Heat Mass Transfer*, 43: 787.
20. Prince, M.J.; Blanch, H.W. (1990) Bubble coalescence and break-up in air-sparged bubble columns. *AIChE J.*, 36 (10): 1485.
21. Ranade, V.V. (2002) *Computational Flow Modeling for Chemical Reactor Engineering*; Academic Press: New York, U.S.A.
22. Ishii, M.; Hibiki, T. (2006) *Thermo Fluid Dynamics of Two-Phase Flow*, 1st Ed.; Springer Science: New York.
23. Antal, S.; Lahey, R., Flaherty, J. (1991) Analysis of phase distribution in fully-developed laminar bubbly two phase flow. *Int. J. Multiphase Flow*, 7: 635.
24. Saboni, A.; Alexandrova, S. (2002) Numerical study of the drag on a fluid sphere. *AIChE J.*, 48 (12): 2992.
25. Burns, A.D.; Frank, T.; Hamill, I.; Shi, J.-M. (2004) The Favre averaged drag model for turbulence dispersion in Eulerian multi-phase flows. *In: Proceedings of the Fifth Int. Conf. on Multiphase Flow, ICMF*, Yokohama, Japan.
26. Versteeg, H.K.; Malalasekera, W. (1995) *An Introduction to Computational Fluid Dynamics, the Finite Volume Method*; Longman Group Ltd: New York.
27. Launder, B.E. (1989) Second-moment closure and its use in modeling turbulent industrial flows. *Int. J. Num. Methods in Fluids*, 9 (8): 963.
28. Slack, M.D.; Del Porte, S.; Engelman, M.S. (2003) Designing automated computational fluid dynamics modeling tools for hydrocyclone design. *Minerals Eng.*, 17: 705.
29. Ko, J.; Zahrai, S.; Macchion, O.; Vomhoff, H. (2006) Numerical modeling of highly swirling flows in a through-flow cylindrical hydrocyclone. *AIChE J.*, 52 (10): 3334.
30. Gomez, C.; Caldenty, J.; Wang, S. (2002) Oil/water separation in liquid/liquid hydrocyclons: Part 1- Experimental investigation. *SPE J.*, 7: 353.